MechanoEngineering

RESEARCH ARTICLE | OCTOBER 12 2026

Modulation of complex Bessel modes by generalized impedance metasurfaces for potential acoustic channels

Yu-Ze Tian ; Zhuo-Run Wei ; Yan-Feng Wang ; Vincent Laude ; Yue-Sheng Wang

Check for updates

MechanoEngineering 1, 043101 (2026)
https://doi.org/10.1063/5.0344561

View Online
Export Citation

Articles You May Be Interested In

Hybrid Bessel beam and metamaterial lenses for deep laparoscopic nondestructive evaluation
J. Appl. Phys. (April 2021)

TE-polarized leaky-wave beam launchers: Generation of Bessel and Bessel–Gauss beams
Appl. Phys. Lett. (October 2024)

Acoustics of finite Bessel tractor beams
J. Acoust. Soc. Am. (September 2015)

24 October 2026 16:30:23

MechanoEngineering
Open for Submissions
No Article Processing Charges (APCs)
Diamond Open Access
Submit Today
AIP Publishing

AIP Publishing

MechanoEngineering RESEARCH ARTICLE pubs.aip.org/nuaa/meg

Featured

Modulation of complex Bessel modes by generalized impedance metasurfaces for potential acoustic channels

Cite as: MechanoEng. 1, 043101 (2026); doi: 10.1063/5.0344561
Submitted: 20 May 2026 • Accepted: 7 September 2026 •
Published Online: 12 October 2026

View Online Export Citation CrossMark

Yu-Ze Tian,[1] Zhuo-Run Wei,[2,3] Yan-Feng Wang,[1,4,a)] Vincent Laude,[5,a)] and Yue-Sheng Wang[1,6]

AFFILIATIONS

[1] School of Mechanical Engineering, Tianjin University, 300350 Tianjin, China
[2] Shanghai Institute of Technical Physics, Chinese Academy of Sciences, Shanghai 200083, China
[3] School of Science, Tianjin University, 300350 Tianjin, China
[4] National Key Laboratory of Vehicle Power System, 300350 Tianjin, China
[5] Université Marie et Louis Pasteur, CNRS, Institut FEMTO-ST, F-25000 Besançon, France
[6] Institute of Engineering Mechanics, Beijing Jiaotong University, Beijing 100044, China

[a)] **Authors to whom correspondence should be addressed:** wangyanfeng@tju.edu.cn and vincent.laude@femto-st.fr

24 October 2026 16:30:23

ABSTRACT

Waves described by Bessel functions of different orders have recently attracted widespread attention. Owing to their potential to provide additional available channels in acoustic communications. Their orthogonality in the azimuthal plane enables spatial multiplexing at a given frequency. The number of available channels is thereby increased, facilitating the development of faster and more reliable communication systems. In this paper, traveling waves with different radial wavenumbers as well as azimuthal indices are employed, leading to a significant increase in potential spatial channels. These waves are termed complex Bessel modes (CBMs) and are rigorously orthogonal when confined within a waveguide. Compared with multiplexing based on orthogonality in the azimuthal plane only, CBMs offer additional spatial degrees of freedom for channel multiplexing. However, a sophisticated requirement on modulation arises naturally, owing to the resulting inhomogeneous amplitude and phase distribution. Generalized impedance metasurfaces are therefore introduced to address this challenge. They convert efficiently between different CBMs, achieving 100% power flow conversion efficiency in numerical simulations. Two demonstration generators for CBMs with zero azimuthal index are fabricated with practical structures obtained through optimization. The input waveguide of the generators can be designed to have one-quarter the cross-sectional area of the output waveguide, owing to the flexibility of the generalized impedance theory. Generation of CBMs can therefore be achieved using a single speaker, eliminating the requirement for a large array of speakers and thereby leading to substantial cost reduction and improved stability. High-purity CBMs are demonstrated in both numerical simulations and experiments. This work reveals the potential of CBMs to serve as additional orthogonal spatial channels for acoustic multiplexing. This extension of generalized impedance theory paves the way for more reliable acoustic communications.

© 2026 Author(s). All article content, except where otherwise noted, is licensed under a Creative Commons Attribution (CC BY) license (https://creativecommons.org/licenses/by/4.0/). https://doi.org/10.1063/5.0344561

I. INTRODUCTION

With the onset of the Information Age, communication technology has played an indispensable role across diverse domains.[1,2] As a nondiffracting transmission mode, Bessel beams[3–5] have aroused considerable enthusiasm for their promising applications in acoustic communications.[6–9] Analogous to carrier technology in the time domain, information is transmitted in terms of spatially modulated Bessel beams of a given frequency, leveraging the orthogonality in the azimuthal plane. Consequently, signals can be carried simultaneously in both time and space, resulting in a significant enhancement of communication efficiency. Nevertheless, long-distance transmission always suffers from dissipation, leading to deficiencies in stability and controllability.[10–12] Similar to

optical fibers,[13,14] acoustic communication systems established within waveguides, also termed acoustic fibers, are attracting substantial attention for this reason.[15,16] Power flux is confined to a definite cross-section, and signal reconstruction can be accomplished by capturing sound pressure along the azimuth.

There are however, two pivotal challenges to be addressed, namely, limitations on available channels and complexity of signal generation. The limited number of available channels appears to be inherently incompatible with miniaturization. Only a finite set of transmission modes can propagate within a waveguide once its radius is selected.[17,18] Additional channels are only available if the radius of the waveguide or the operating frequency can be increased, diverging from the original intention. Furthermore, a large speaker array is required for the generation of sound waves with spiral wavefronts. Each individual speaker in the array needs to be meticulously tailored to provide a specific amplitude and phase.[19–21] This requirement becomes more stringent for modes with larger azimuthal indices or higher frequency.[22,23] Even for the fundamental plane wave, amplitude and phase consistency across speakers in the array remains essential.

Some strategies for exploring available channels have emerged recently. Acoustic spin can be detected in the sound field and described by the local velocity.[24–26] It offers additional degrees of freedom when combined with orbital angular momentum. However, this addition imposes new requirements on the signal generator, which needs to provide a specific polarization. By altering the topology of the waveguide, more channels can be supported by a cylindrical shell waveguide.[27,28] Multiple shell waveguides can hence be nested together to augment information capacity at a given scale length. Nonetheless, each waveguide demands a precisely modulated sound source array. In general, such strategies introduce new difficulties in signal generation.

Acoustic metasurfaces,[29,30] as a type of metamaterial,[31] are widely acknowledged for their exceptional functionality and extreme flexibility. They are recognized as viable candidates for generators or converters of spiral acoustic waves in both free-space systems and waveguides.[32] By discretizing a metasurface into units and arranging them in accordance with the generalized Snell's law,[33–35] control over the azimuthal index of a spiral wave can be achieved through a local phase shift.[17,36] Alternatively, a holistically designed metasurface based on diffraction metagratings[37,38] enables the generation of single[39,40] or combined[41,42] spiral waves of varying azimuthal indices. Furthermore, exotic applications such as directional communication[43] and acoustic diodes[44,45] have been successfully demonstrated. Recently, encrypted information storage[28] has been achieved in a multiplex communication systems based on a newly proposed impedance theory.[46–48] This theory exhibits potential for acoustic communications, owing to its exceptional ability to manipulate waves with precision.[49]

In this paper, generalized impedance metasurfaces are explored for the modulation of complex Bessel modes (CBMs) to access additional orthogonal spatial channels. CBMs constitute a set of mutually orthogonal transmission modes that are characterized by different radial wavenumbers but can share the same azimuthal index. The decomposition of CBM-based signals can be effectively executed on the cross-section when they are constrained within waveguides. This approach results in a significant increase in available channel, surpassing approaches based on spiral waves. Generalized impedance theory is introduced to synergistically modulate amplitude and phase in space. Conversion between CBMs is demonstrated using generalized impedance metasurfaces through numerical simulations that reveal a precise modulation capability. Furthermore, two metasurfaces with zigzag structures are fabricated for practical generation of different CBMs with zero azimuthal index. Generalized impedance metasurfaces are also improved. The input diameter of the metasurfaces is designed to be smaller than the output diameter, enabling signal generation from a single speaker. Operation is validated with both simulations and experiments, demonstrating filtering characteristics for pure transmission fields. It is expected that this work can open up new horizons for the application of impedance theory and CBMs to acoustic communications.

II. COMPLEX BESSEL MODES IN WAVEGUIDES

The definition of metasurfaces has often imposed the constraint that the cross-sections of interconnected sound fields p_1 and p_2 be equal. This constraint leads to the requirement for a considerable array of sound sources, particularly when the aim is to modulate waves combining multiple modes. Such a scenario thus presents significant challenges for the control circuit of the speakers, even for the generation of a simple plane wave. Ensuring consistency across the speakers of a coherent array introduces an extra layer of complexity. Fortunately, generalized impedance theory theoretically allows the design of metasurfaces that operate under the conditions illustrated in Fig. 1. It is anticipated that the cross-sectional area of the field p_1 is narrow enough for the incident field to be excited with a single speaker. Meanwhile, the transmission field p_2 will encompass multiple, mutually orthogonal, independent transmission modes. Subsequently, digital information can be precisely encoded in the field p_2 and retrieved through a process of signal decomposition.

Let us start with a general analysis of acoustic waves in a circular waveguide. Helmholtz's equation with sound pressure p as the variable is adopted to describe the acoustic fields:

$$\left(\nabla^2 + \omega_0^2/c_0^2\right)p = 0, \tag{1}$$

where $\omega_0 = 2\pi f_0$ is the operating angular frequency, f_0 is the operating frequency in Hz, $c_0 = \sqrt{K_0/\rho_0}$ is the velocity of sound in the homogeneous background medium, and ρ_0 and K_0 are its mass density and bulk modulus, respectively. Bessel solutions can be obtained using the method of separation of variables in cylindrical coordinate (ρ, θ, z). Then, the lth solution for the mth order (the integer m is the azimuthal index) is written

$$p_{l,m}(\rho, \theta, z) = D_{l,m} J_m(\beta_{l,m}\rho) \mathrm{e}^{-\imath\alpha_{l,m}z - \imath m\theta - \imath\varphi_{l,m}}, \tag{2}$$

where $\imath$ is the imaginary unit, J_m is the mth Bessel function of the first kind, and $D_{l,m}$ and $\varphi_{l,m}$ are the amplitude and phase, respectively. The real-valued wavenumbers $\alpha_{l,m}$ and $\beta_{l,m}$ obey the dispersion relation

$$\alpha_{l,m}^2 + \beta_{l,m}^2 = k_0^2, \tag{3}$$

where $k_0 = \omega/c_0$ is the wavenumber in the background medium. Here, $\alpha_{l,m}$ is the axial wavenumber and $\beta_{l,m}$ can be regarded as the radial wavenumber corresponding to $\alpha_{l,m}$. It is shown below that the axial wavenumber is quantized.

24 October 2026 16:30:23

© Author(s) 2026

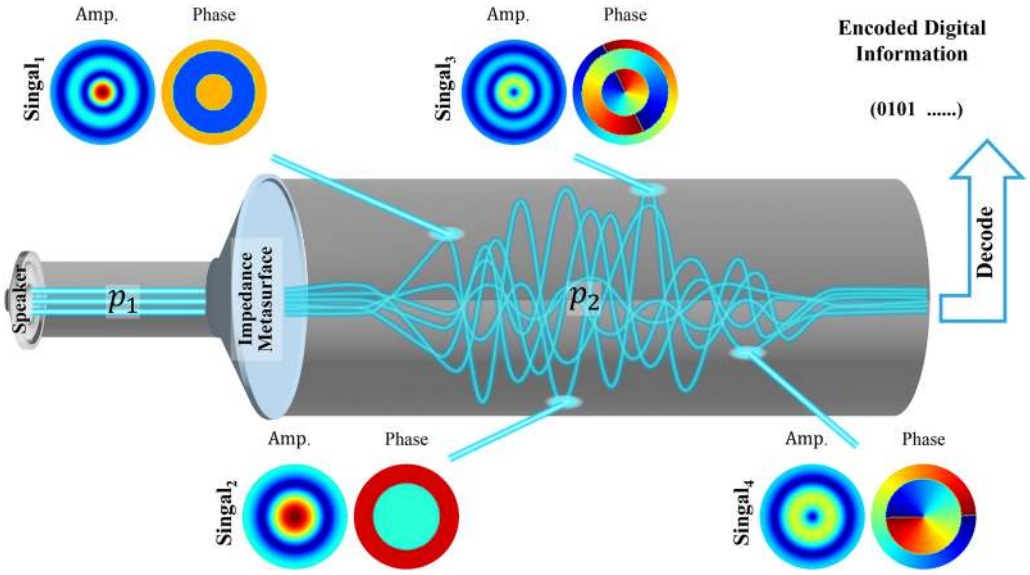


FIG. 1. Illustration of a generalized impedance metasurface for CBM generation. A metasurface with two unequal cross-sectional areas connects a fundamental planar wave field p_1 generated by a speaker and a field p_2 encoded with specific digital information through amplitude and phase modulation.

The superposition of waves with a specific azimuthal index m is described by

$$p_m(\rho,\theta,z) = \sum_l p_{l,m}(\rho,\theta,z) = \sum_l C_{l,m}(\rho,z)\mathrm{e}^{-\imath m\theta}. \tag{4}$$

Generally, orthogonality is verified strictly along any circular curve $(\rho,z) = (\rho_0,z_0)$ for different azimuthal indices $m_1, m_2 \in \mathbb{Z}$:

$$\oint_{(\rho_0,z_0)} p_{m_1} p^*_{m_2}\,\mathrm{d}\theta = 0 \quad \text{if } m_1 \neq m_2. \tag{5}$$

It is noteworthy, however, that there can be several waves distinguished by different axial and radial wavenumbers but the same azimuthal index. Despite those waves traveling stably along the axial direction, they are generally considered to degrade purity.[18] Such waves are the primary focus of the following study and are termed complex Bessel modes (CBMs).

For CBMs constrained within a waveguide, for example, an acoustic fiber,[15] a hard acoustic boundary condition is added at $\rho = R_0$:

$$\left.\frac{\partial p}{\partial \rho}\right|_{\rho=R_0} = 0, \tag{6}$$

where R_0 is the inner radius of the waveguide. Since Eq. (6) holds everywhere at $\rho = R_0$, the defining relation for each $\beta_{l,m}$ reads

$$J'_m(\beta_{l,m}R_0) = 0, \tag{7}$$

i.e., $\beta_{l,m}$ is obtained from the roots of the first derivative of the Bessel function J_m. There are a finite number of solutions to Eq. (7), since $0 \le \beta_{l,m} \le k_0$ from Eq. (3); these solutions can be retrieved numerically using, for instance, the Newton iteration method.

For illustration, we consider the example of CBMs in a waveguide with a given radius $R_0 = 15$ cm. The background medium is taken to be air, with a sound velocity $c_0 = 343$ m/s, mass density $\rho_0 = 1.18$ kg/m^3, and zero viscosity. The operating frequency is chosen as $f_0 = 3500$ Hz. The wavelength and wavenumber of sound waves in the background field are $\lambda_0 = c_0/f_0$ and $k_0 = 2\pi/\lambda_0$, respectively. Traveling wave solutions along the positive z axis require $\alpha_{l,m} > 0$. The allowed CBMs and corresponding parameters are given in Table I.

It might be assumed that 15 multiplexed channels are supported by this waveguide,[32] since $|m_{\max}| = 7$, as indicated in Table I. However, this number only includes modes with $l = 1$. There can actually be two (for $m = \pm2, \pm3, \pm4$) or even three (for $m = 0, \pm1$) independent transmission modes with the same m, for a total of 27 CBMs. Taking the three CBMs for $m = 0$ as examples, the real part of the complex amplitude distributions defined by Eq. (2) are depicted in Fig. 2. The transmission mode degenerates into a plane wave when $\beta_{1,0} = 0$ m^{-1} in Fig. 2(a). However, for $\beta_{2,0} = 25.5$ m^{-1}, the wavefront remains planar but carries an inhomogeneous amplitude distribution, as shown in Fig. 2(b). Its amplitude first decreases and subsequently increases along the radius, following the variations of the Bessel function. A similar situation is observed in Fig. 2(c). The amplitude changes faster along the radial direction as the radial wavenumber is increased to $\beta_{3,0} = 46.8$ m^{-1}. Notably, two nodes of pressure can be identified, and the sign of the amplitude changes twice. Furthermore, the period along the z axis decreases with l, which indicates a decrease in the axial wavenumber $\alpha_{l,m}$. For an intuitive illustration, the amplitude distribution along the radius is plotted in Fig. 2(d). All CBMs follow the zeroth-order Bessel function, with the plane wave considered as a special trivial form.

CBMs with $m = +1$ are also depicted in Fig. 2 for comparison. Each mode exhibits a periodicity, characterized by a period of

24 October 2026 16:30:23

© Author(s) 2026

TABLE I. Allowed CBMs for a waveguide with radius R_0 = 15 cm, at operating frequency f_0 = 3500 Hz.

	$\beta_{l,m}$ (m^{-1})							
	$m = 0$	±1	±2	±3	±4	±5	±6	±7
$l = 1$	0	12.3	20.4	28.0	35.5	42.8	50.0	57.2
$l = 2$	25.5	35.5	44.7	53.4	61.9	/	/	/
$l = 3$	46.8	56.9	/	/	/	/	/	/

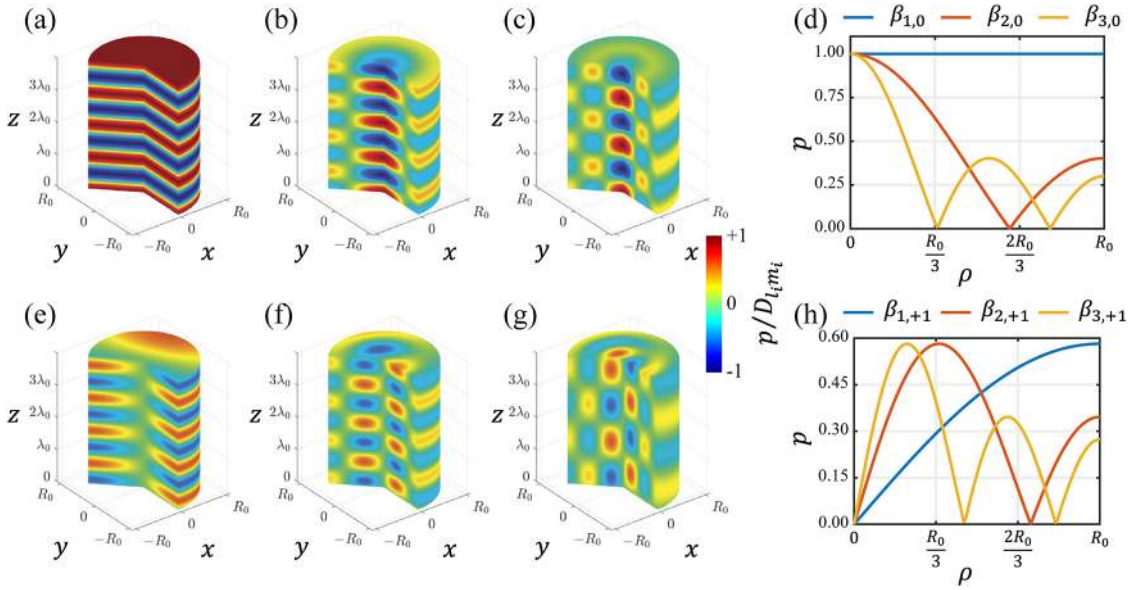


FIG. 2. Theoretical spatial distribution of normalized sound pressure for traveling CBMs with azimuthal index $m = 0$ and [(a)–(d)] $m = +1$ [(e)–(h)]. (a)–(c) CBMs with $m = 0$ and radial wavenumbers $\beta_{1,0} = 0$ m^{-1}, $\beta_{2,0} = 25.5$ m^{-1}, and $\beta_{3,0} = 46.8$ m^{-1}, respectively. (d) Amplitude distributions along the radius ρ for CBMs with $m = 0$ and $\beta_{1,0} = 0$ m^{-1} (blue curve), $\beta_{2,0} = 25.5$ m^{-1} (red curve), and $\beta_{30} = 46.8$ m^{-1} (orange curve). (e)–(g) CBMs with $m = +1$ and radial wavenumbers $\beta_{1,+1} = 12.3$ m^{-1}, (f) $\beta_{2,+1} = 35.5$ m^{-1}, and (g) $\beta_{3,+1} = 56.9$ m^{-1}, respectively. (h) Amplitude distribution along the radius ρ for CBMs with $m = +1$ and $\beta_{1,+1} = 12.3$ m^{-1} (blue curve), $\beta_{2,+1} = 35.5$ m^{-1} (red curve), and $\beta_{3,+1} = 56.9$ m^{-1} (orange curve).

1 along the azimuthal direction. The CBM with $\beta_{1,+1} = 12.3$ m^{-1} in Fig. 2(e) degenerates into a wave with spiral phase distribution as previously reported.[17] Both CBMs in Figs. 2(e) and 2(f) have the same spiral phase distribution. Similar to the case $m = 0$, their amplitude varies nonmonotonically with radius when $l \neq 1$. The axial wavenumber decreases as the radial wavenumber increases, in accordance with Eq. (3). The amplitude distribution along the radius is plotted in Fig. 2(h). All CBMs follow the first-order Bessel function.

All the above CBMs are naturally orthogonal, since they are fundamental solutions of the governing equation, Eq. (2). Each mode can be regarded as an independent channel with stable transmission capability. It is obvious that orthogonal decomposition can be conducted along the axial direction, owing to differences in axial periods. It can also be proved that modes involving the same Bessel function but different zeros of its first derivative are actually orthogonal (see Appendix A). All the 27 modes listed in Table I can be fully decomposed on any cross-section of the waveguide. This allows for the support of 27 multiplexed spatial channels, as opposed to 15 channels, which may lead to a substantial improvement for acoustic communication.

III. CONVERSION BETWEEN CBMs BY GENERALIZED IMPEDANCE METASURFACES

Owing to a lack of control of the amplitude, gradient metasurfaces based on the generalized Snell's law are generally not well suited to conversion between CMBs. Similarly, a precise customization of the wave amplitude distribution is difficult with metagratings. As an alternative, generalized impedance theory is adopted in this section. Generalized impedance metasurfaces transform arbitrary wave fields.[49] Through meticulous structural design, it is theoretically feasible to establish a connection between fields of unequal cross-section, as illustrated in Fig. 1. When the radius of the input

24 October 2026 16:30:23

© Author(s) 2026

waveguide is sufficiently small, generation of CBMs can be accomplished through the operation of a single speaker cooperating with a metasurface.

For generality, it is necessary to ensure first the validity of generalized impedance theory for CBM conversion. Conversion between different CBMs inside waveguides of equal width is examined in this section through numerical simulation with a single-layer model of impedance metasurface. It is assumed that two fields p_1 and p_2 are connected through an impedance metasurface, as shown in Fig. 1. The local velocities $\mathbf{v}_i = (\imath/\omega_0\rho_0)\nabla p_i$ and power flux distributions $\mathbf{I}_i = \frac{1}{2}\mathrm{Re}\left[p_i\mathbf{v}_i^*\right]$ $(i = 1, 2)$ are obtained from Eq. (2). For a passive and lossless metasurface, a loose conservation of power flux is imposed through

$$\int_{\Gamma_1} \mathbf{I}_1 \cdot \mathbf{n}_1 \mathrm{d}S + \int_{\Gamma_2} \mathbf{I}_2 \cdot \mathbf{n}_2 \mathrm{d}S = 0, \tag{8}$$

where the surfaces Γ_i $(i = 1, 2)$ are the upper and lower boundaries of the metasurface, and the normal vectors $\mathbf{n}_i$ $(i = 1, 2)$ point toward the interiors of the outer regions. Assuming that the metasurface is located in the $y = 0$ plane, its impedance is determined as

$$\begin{bmatrix} p_1 \\ p_2 \end{bmatrix}\Big|_{y=0} = \begin{bmatrix} Z_{11} & Z_{12} \\ Z_{21} & Z_{22} \end{bmatrix}\begin{bmatrix} (-\mathbf{n}_1 \cdot \mathbf{v}_1) \\ (-\mathbf{n}_2 \cdot \mathbf{v}_2) \end{bmatrix}\Big|_{y=0}. \tag{9}$$

For a conservative system, the impedance matrix is purely imaginary:

$$Z_{ik} = \imath X_{ik} \tag{10}$$

with a real matrix X_{ik}.

For CBM conversion from mode (l_1, m_1) to mode (l_2, m_2), the sound fields on the two sides of the metasurface are

$$p_1(\rho, \theta, z) = D_{l_1,m_1} J_{m_1}(\beta_{l_1,m_1}\rho)\mathrm{e}^{-\imath\alpha_{l_1,m_1}z - \imath m_1\theta - \imath\varphi_{l_1,m_1}}, \tag{11}$$

$$p_2(\rho, \theta, z) = D_{l_2,m_2} J_{m_2}(\beta_{l_2,m_2}\rho)\mathrm{e}^{-\imath\alpha_{l_2,m_2}z - \imath m_2\theta - \imath\varphi_{l_2,m_2}}, \tag{12}$$

respectively. The amplitudes obey Eq. (8), and hence the amplitude factor is given by

$$A = \frac{D_{l_2,m_2}}{D_{l_1,m_1}} = \sqrt{\frac{\alpha_{l_1m_1}(\beta_{l_1,m_1}^2 R_0^2 - m_1^2)}{\alpha_{l_2,m_2}(\beta_{l_2,m_2}^2 R_0^2 - m_2^2)}}\frac{\beta_{l_2,m_2}|J_{m_1}(\beta_{l_1,m_1}R_0)|}{\beta_{l_1,m_1}|J_{m_2}(\beta_{l_2,m_2}R_0)|}. \tag{13}$$

The components of the impedance matrix in Eq. (9) can be calculated as

$$Z_{11}(\theta) = -\frac{\imath Z_0 k_0}{\alpha_{l_1,m_1}}\cot\Phi(\theta), \tag{14}$$

$$Z_{12}(\rho, \theta) = -\frac{\imath Z_0 k_0}{\alpha_{l_2,m_2} A}\frac{J_{m_1}(\beta_{l_1,m_1}\rho)}{J_{m_2}(\beta_{l_2,m_2}\rho)}\csc\Phi(\theta), \tag{15}$$

$$Z_{21}(\rho, \theta) = -\frac{\imath Z_0 k_0 A}{\alpha_{l_1,m_1}}\frac{J_{m_2}(\beta_{l_2,m_2}\rho)}{J_{m_1}(\beta_{l_1,m_1}\rho)}\csc\Phi(\theta), \tag{16}$$

$$Z_{22}(\theta) = -\frac{\imath Z_0 k_0}{\alpha_{l_2,m_2}}\cot\Phi(\theta), \tag{17}$$

where

$$\Phi(\theta) = (m_2 - m_1)\theta + (\varphi_{l_2,m_2} - \varphi_{l_1,m_1}). \tag{18}$$

It should be noted that the amplitude factor will reduce to

$$A = \frac{D_{l_2,m_2}}{D_{l_1,m_1}} = \sqrt{\frac{k_0}{\alpha_{l_2,m_2}R_0^2(\beta_{l_2,m_2}^2 R_0^2 - m_2^2)}}\frac{\beta_{l_2,m_2}}{|J_{m_2}(\beta_{l_2,m_2}R_0)|} \tag{19}$$

when a plane wave is incident.

There is a unified formal expression of the impedance matrix for conversion between two CBMs. The components on the main diagonal vary with the azimuth, whereas the components on the secondary diagonal vary with the radius. The impedance matrix is independent of the azimuth when the azimuthal indices of the CBMs are identical $(m_1 = m_2)$. The components on the main diagonal then become constant and are determined by the phase difference $\varphi_{l_2,m_2} - \varphi_{l_1,m_1}$. They tend to infinity when $\varphi_{l_2,m_2} = \varphi_{l_1,m_1}$, which is physically valid. It has indeed been proved that a singular impedance can be achieved via an appropriate modulation of phase and amplitude.[48] Since the impedance matrix is purely imaginary, conversion between arbitrary CBMs is achieved by passive metasurfaces.[46] The components on the secondary diagonal are always unequal. This indicates that a balance of the power flux needs to be implemented under integral equivalence.[49] Then, the cross-sectional areas on each side of each unit of the metasurface are unequal in the subsequent structural design.

We consider the generalized metasurfaces defined by Eqs. (14)–(17) to be ideally devoid of thickness to check their theoretical performance as illustrated in Fig. 3 (see Appendix B for detailed settings). It should be noted that the amplitude factor in Eq. (13) is not unitary, which means that conversion between different CBMs is accompanied by changes in amplitude. All figures are therefore normalized to their respective amplitudes for the purpose of comparison. The generation of the CBM with $\beta_{2,0}$ via plane wave excitation is demonstrated first in Fig. 3(a). The incident field remains uncontaminated by any reflected waves. The transmission field agrees with the theoretical result presented in Fig. 2(a). It can be observed that all of the power flux has been allocated to the target CBM without any crosstalk toward other CBMs (see Appendix C for the detailed quantitative analysis). A similar situation is observed for the generation of the CBM with $\beta_{3,0}$ as shown in Fig. 3(b). There is no scattering on either side of the metasurface. Furthermore, the orthogonal decomposition confirms the exact operation of the metasurface.

Let us move on to the conversion between different CBMs. Conversion from the CBM with $\beta_{3,0}$ to that with $\beta_{2,0}$ is shown in Fig. 3(c). The amplitude of the wave field on both sides follows the Bessel distribution, with the orthogonal decomposition indicating a conversion rate of 100%. Numerical simulations for conversion between different CBMs with +1 azimuthal index are presented in Figs. 3(d) and 3(e). They appear somewhat similar to Fig. 3(c) because the conversion between CBMs with the same azimuthal index is always independent of the azimuth [Eq. (18)]. There is only a difference in the impedance distribution along the radius. The conversion remains perfect, as indicated by the orthogonal decomposition. This result remains even if the impedance changes with the azimuthal angle when conversion is from the CBM with $\beta_{3,+1}$

24 October 2026 16:30:23

© Author(s) 2026

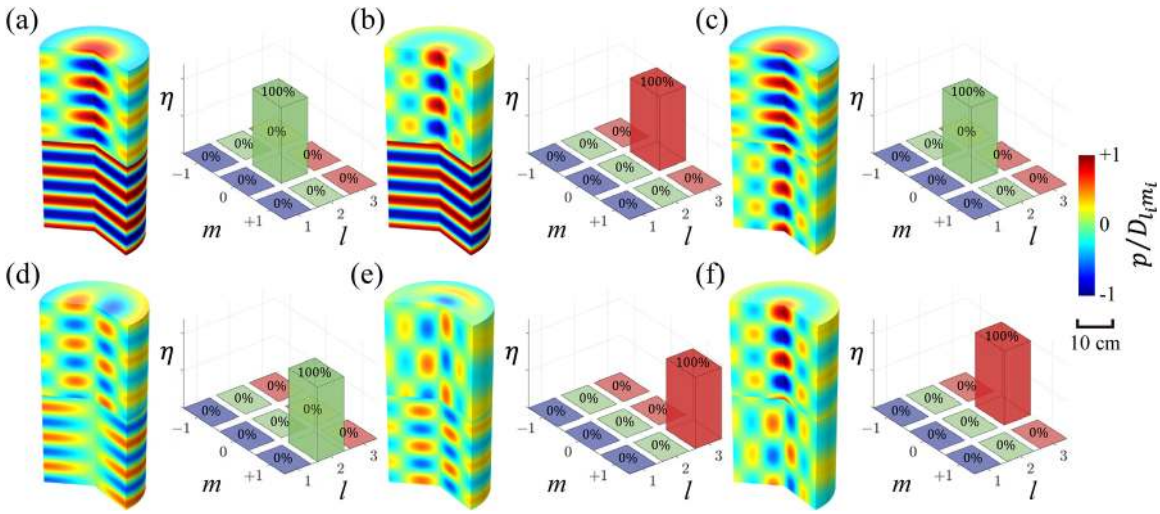


FIG. 3. Verification by numerical simulation of the operation of metasurfaces for CBM conversion. Normalized total pressure fields and orthogonal decompositions of the output signal are shown for conversion (a) from $\beta_{1,0}$ to $\beta_{2,0}$, (b) from $\beta_{1,0}$ to $\beta_{3,0}$, (c) from $\beta_{2,0}$ to $\beta_{3,0}$, (d) from $\beta_{1,+1}$ to $\beta_{2,+1}$, (e) from $\beta_{2,+1}$ to $k_{3,+1}$, and (f) from $\beta_{3,+1}$ to $\beta_{3,0}$.

to that with $\beta_{3,0}$, as shown in Fig. 3(f). In practice, the fabrication of metasurfaces for conversion between CBMs with different azimuthal indices is potentially trickier, since both azimuth and radial directions must be considered simultaneously.

IV. STRUCTURAL DESIGN OF CBM GENERATORS AND EXPERIMENTAL VALIDATION WITH SINGLE SPEAKER EXCITATION

For easier generation of CBMs with a single speaker, the input waveguide must have a smaller radius than the output waveguide. This adjustment results in fewer transmission modes within the input waveguide,[18] thereby simplifying the process of plane wave excitation. The design of conventional metasurfaces, however, requires two physical fields of equal spatial extent. Generalized impedance metasurfaces are more flexible in this respect and are adopted for implementation here. The output waveguide is set to have a radius of $R_o = R_0 = 15$ cm, as mentioned earlier. The radius of the input waveguide is set to $R_i = R_0/2 = 7.5$ cm. Two examples are considered in this section, with the generation of CBMs with $\beta_{2,0}$ and $\beta_{3,0}$ under plane wave input. The generalized impedance unit obeys the discrete impedance relation

$$\begin{bmatrix} \bar{p}_1|_{D_1^j} \\ \bar{p}_2|_{D_2^j} \end{bmatrix} = \begin{bmatrix} Z_{11}^j & Z_{12}^i \\ Z_{21}^j & Z_{22}^i \end{bmatrix} \begin{bmatrix} (-\bar{\mathbf{n}}_1 \cdot \bar{\mathbf{v}}_1)|_{D_1^j} \\ (-\bar{\mathbf{n}}_2 \cdot \bar{\mathbf{v}}_1)|_{D_2^j} \end{bmatrix}, \tag{20}$$

where D_i^j $(i = 1, 2)$ are the jth subdomains of Γ_i $(i = 1, 2)$, and $\bar{p}_i, \bar{\mathbf{n}}_i$ and $\bar{\mathbf{v}}_i$ $(i = 1, 2)$ are the average values on D_i $(i = 1, 2)$. The division of D_i $(i = 1, 2)$ is in line with the principles established in Ref. 49. The two generalized impedance metasurfaces presented in Fig. 4(a) are obtained through optimization and consist of nine zigzag units each (see Appendix D).

Numerically simulated pressure fields for the designed generalized impedance metasurfaces are presented in Fig. 4(b) (see Appendix B for detailed settings). Generation of the target CBMs is evident, despite some minor reflections on the input side. A quantitative evaluation through orthogonal decomposition of the output signal is given in Fig. 4(c) (see Appendix C for the detailed quantitative analysis). The power flux is precisely allocated to the target mode for the CBM with $\beta_{2,0}$, and only 1% is leaked. The result for the CBM with $\beta_{3,0}$ is not ideal, however, since only 88% of the power flux is converted successfully. The discretization of metasurface units is likely the major reason for this discrepancy. Generalized impedance theory indeed requires the unit to be deeply sub-wavelength, but a sufficient span of geometric parameters is also essential for the unit to approach the theoretical impedance matrix. These conflicting requirements may lead to an operational trade-off. A discussion of the influence of the discretization of units on efficiency is provided in Appendix E. Nevertheless, the overall operation is acceptable for CBM generation.

Two samples were fabricated using 3D printing for experimental verification, as shown in Fig. 4(d). Each metasurface is assembled from two distinct parts. An additional support runs across the middle of each part to ensure the stability of the structure. The distribution of the real part of the experimental sound pressure field is shown in Fig. 4(e). The sound field at the input end is provided by a single speaker with radius 7.5 cm (see Appendix F for the detailed configuration). All fields have been normalized with reference to the average amplitude of the incident wave. Good consistency between Figs. 4(b) and 4(e) is observed visually. Although the spatial distribution of amplitude is generally consistent with expectations, the experimental amplitude is smaller than in the numerical simulation. This is even more true for the generation of the $\beta_{3,0}$ CBM. Note that the pressure amplitude fluctuates along the z axis owing to interference of CBMs with different axial wavenumbers. The total transmitted

24 October 2026 16:30:23

© Author(s) 2026

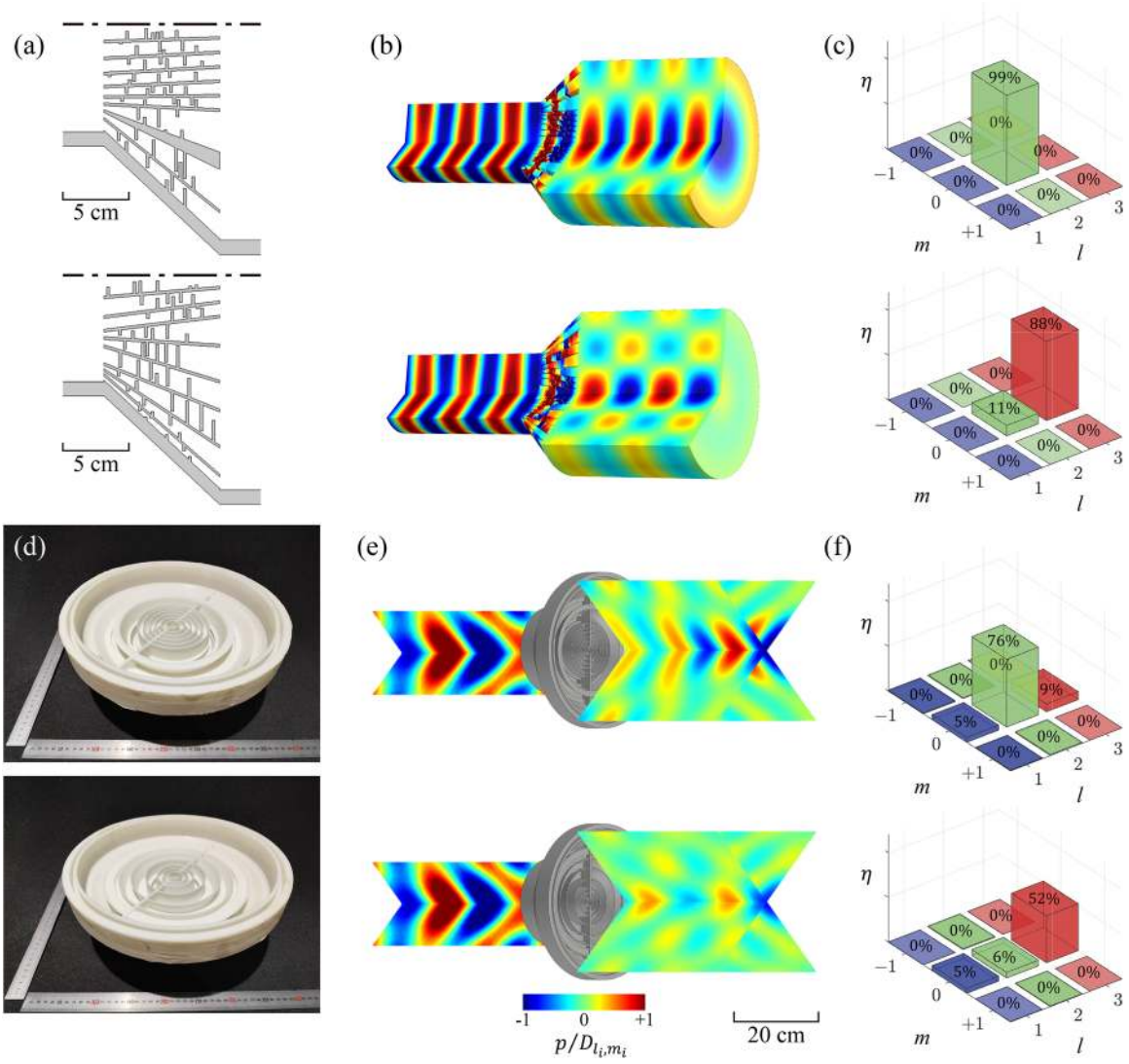


FIG. 4. Verification by numerical simulation and experiment of metasurfaces designed for CBM generation from a plane wave to CBMs with $\beta_{2,0}$ and $\beta_{3,0}$. The metasurface designed by optimization (a) produces the simulated pressure field in (b). whose orthogonal decomposition is shown in (c). The fabricated metasurface (d) produces the experimental pressure field in (e), whose orthogonal decomposition is shown in (f).

power flux does not reach 100% experimentally, as can also be seen from the quantitative analysis in Fig. 4(f). In the generation of the CBM with $\beta_{2,0}$, 76% of the power flux is successfully delivered, whereas 52% is delivered in the generation of the CBM with $\beta_{3,0}$. Fabrication tolerances and the presence of additional supports in the middle of the structure may partially explain the decrease in efficiency. Moreover, it can be seen that the incident wave is not strictly plane. The wavefront generated by the single speaker has some curvature, leading to the excitation of some other complex modes in the input waveguide. The additional reflection on the speaker may also cause unpredictable disturbances. However, the target CBMs dominate both output signal, thanks to the inherent characteristics of generalized impedance metasurfaces operating as filters.[28] Only preset modes can be transmitted effectively, which may be beneficial for the establishment of CBM-based communication systems. Discussions of operating frequencies and of the influence of nonplanar excitation for both designed metasurfaces are provided in Appendixes G and H, respectively, with thermal viscosity accounted for.

This section has presented the generic design of a CBM with an azimuthal index of $m = 0$ based on generalized impedance theory. However, it is noteworthy that considering a nonzero azimuthal

24 October 2026 16:30:23

© Author(s) 2026

index may still lead to great complexity if CBMs with $m \neq 0$ are expected to be directly generated through a generalized impedance metasurface with a single speaker. The design of impedance units must be executed in three dimensions, with all feature sizes being deeply sub-wavelength. For example, for the waveguide considered in this paper, the metasurface should be discretized into at least 185 units, provided that the maximum feature size of each unit is 3 cm. Hence, the design and manufacture of the structure will become the major challenge, although it can still be implemented theoretically.[48,49]

V. DISCUSSION

In this paper, orthogonal CBMs have been investigated as potential available channels of acoustic fiber communication systems enabled by generalized impedance theory. Not only the azimuthal indices m but also the radial indices l have been considered as multiplexing degrees of freedom. Generalized impedance theory has been employed for the conversion of CBMs. The operational efficiency consistently reaches 100%, as verified through thickness-free models of the metasurfaces in simulation. Furthermore, two practical metasurfaces with optimized unit structures have been designed for the generation of CBMs with azimuthal index $m = 0$ but different radial indices. A generalized impedance metasurface between two different waveguides has been established for the first time. The areas of the input waveguides for both metasurfaces are one-quarter of the output one, thanks to the flexibility afforded by generalized impedance theory. Consequently, the designed generalized impedance metasurfaces offer a convenient means of signal generation via a single speaker, as opposed to an array of sound sources. Their operation has been validated both numerically and experimentally. The generated signal remains a pure mode, even when the incident wave in the experiment is not strictly planar.

CBMs exhibit immense potential for acoustic communications, especially when harnessed through generalized impedance metasurfaces. The number of potential available channels within the waveguide is significantly increased by the use of all available modes of propagation. Moreover, signal generation can be streamlined at a relatively low cost. Additionally, the excitation of incident plane waves can be further simplified if the radius of the input waveguide is sufficiently reduced, since only waves other than plane waves are accommodated and the incident wave becomes purely planar. Nevertheless, the significant contrast that is required between input and output waveguide cross-sections may pose substantial challenges for structural fabrication. Specifically, fabrication tolerances and internal structural supports may become key challenges for optimizing the efficiency of metamaterials suitable for conversion between CBMs with different azimuthal indices. Subsequent work will be devoted to expanding the operating bandwidth of generalized impedance metasurfaces and investigating the application of CBMs to free-space emission.

ACKNOWLEDGMENTS

The authors acknowledge financial support by the National Natural Science Foundation of China (Grant Nos. 124B2034 and 12021002). V.L. acknowledges financial support by the EIPHI Graduate School (Grant No. ANR-17-EURE-0002).

AUTHOR DECLARATIONS

Conflict of Interest

The authors have no conflicts to disclose.

Author Contributions

Yu-Ze Tian: Funding acquisition (equal); Investigation (equal); Methodology (equal); Resources (equal); Software (equal); Writing – original draft (equal). **Zhuo-Run Wei**: Data curation (equal); Investigation (equal); Software (equal). **Yan-Feng Wang**: Conceptualization (equal); Funding acquisition (equal); Resources (equal); Supervision (lead); Writing – review & editing (equal). **Vincent Laude**: Formal analysis (equal); Writing – review & editing (equal). **Yue-Sheng Wang**: Funding acquisition (equal); Resources (equal); Writing – review & editing (equal).

DATA AVAILABILITY

The data that support the findings of this study are available from the corresponding authors upon reasonable request.

APPENDIX A: PROOF OF ORTHOGONALITY OF CBMs

According to the Lommel integral, we obtain

$$I = (a^2 - b^2)\int_0^P J_m(a\rho)J_m(b\rho)\rho\,\mathrm{d}\rho = P[bJ_m(aP)J_m'(bP) - aJ_m'(aP)J_m(bP)], \tag{A1}$$

where $a \neq b$ and J_m' is the derivative of the mth-order Bessel function. We set $a = \beta_{l_1,m}$, $b = \beta_{l_2,m}$, and $P = R_0$, and then

$$I = R_0\left[\beta_{l_2,m}J_m(\beta_{l_1,m}R_0)J_m'(\beta_{l_2,m}R_0) - \beta_{l_1,m}J_m'(\beta_{l_1,m}R_0)J_m(\beta_{l_2,m}R_0)\right]. \tag{A2}$$

From Eq. (7), this expression is clearly equal to 0, and so

$$\int_0^{R_0} J_m(\beta_{l_1,m}\rho)J_m(\beta_{l_2,m}\rho)\rho\,\mathrm{d}\rho = 0. \tag{A3}$$

Let us next consider $a = \beta_{l,m}$ and $b = a + \epsilon/R_0$ next, where ϵ is a positive small quantity. We obtain

$$I = \frac{-2R_0\beta_{l,m}\epsilon + o(\epsilon^2)}{R_0^2}\int_0^{R_0} J_m(\beta_{l,m}\rho)J_m\left[\left(\beta_{l,m} + \frac{\epsilon}{R_0}\right)\rho\right]\rho\,\mathrm{d}\rho = (R_0\beta_{l,m} + \epsilon)J_m(\beta_{l,m}R_0)J_m'(R_0\beta_{l,m} + \epsilon) - R_0\beta_{l,m}J_m'(\beta_{l,m}R_0)J_m(R_0\beta_{l,m} + \epsilon). \tag{A4}$$

24 October 2026 16:30:23

© Author(s) 2026

Using a Taylor expansion of $J'_m(R_0\beta_{l,m}+\epsilon)$ as

$$J'_m(R_0\beta_{l,m}+\epsilon)=J'_m(R_0\beta_{l,m})+J''_m(R_0\beta_{l,m})\epsilon+o(\epsilon^2), \tag{A5}$$

we have

$$\begin{aligned} I=&\frac{-2R_0\beta_{l,m}\epsilon+o(\epsilon^2)}{R_0^2}\int_0^{R_0}J_m(\beta_{l,m}\rho)J_m\left[\left(\beta_{l,m}+\frac{\epsilon}{R_0}\right)\rho\right]\rho\,\mathrm{d}\rho\\ =&(R_0\beta_{l,m}+\epsilon)J_m(\beta_{l,m}R_0)J'_m(R_0\beta_{l,m})\\ &+\epsilon(R_0\beta_{l,m}+\epsilon)J_m(\beta_{l,m}R_0)J''_m(R_0\beta_{l,m})\\ &-R_0\beta_{l,m}J'_m(\beta_{l,m}R_0)J_m(R_0\beta_{l,m}+\epsilon). \end{aligned} \tag{A6}$$

Using Eq. (7), and eliminating high-order small quantities, this can be simplified to

$$\begin{aligned} &\frac{-2R_0\beta_{l,m}\epsilon}{R_0^2}\int_0^{R_0}J_m(\beta_{l,m}\rho)J_m\left[\left(\beta_{l,m}+\frac{\epsilon}{R_0}\right)\rho\right]\rho\,\mathrm{d}\rho\\ &=\epsilon R_0\beta_{l,m}J_m(\beta_{l,m}R_0)J''_m(\beta_{l,m}R_0). \end{aligned} \tag{A7}$$

We then get

$$\int_0^{R_0}J_m(\beta_{l,m}\rho)J_m(\beta_{l,m}\rho)\rho\,\mathrm{d}\rho=-\frac{R_0^2}{2}J_m(\beta_{l,m}R_0)J''_m(\beta_{l,m}R_0). \tag{A8}$$

Orthogonality follows as a consequence:

$$\int_0^{R_0}J_m(\beta_{l_1,m}\rho)J_m(\beta_{l_2,m}\rho)\rho\,\mathrm{d}\rho=\begin{cases}0 & \text{if}\quad \beta_{l_1,m}\neq\beta_{l_2,m},\\ \dfrac{\beta_{l_0,m}^2R_0^2-m^2}{2\beta_{l_0,m}^2}[J_m(\beta_{l_0,m}R_0)]^2 & \text{if}\quad \beta_{l_1,m}=\beta_{l_2,m}=\beta_{l_0,m}\neq 0,\\ \dfrac{R_0^2}{2} & \text{if}\quad \beta_{l_1,m}=\beta_{l_2,m}=0.\end{cases} \tag{A9}$$

Note that $\beta_{l_1,m}=\beta_{l_2,m}=0$ implies $m=0$.

APPENDIX B: SIMULATIONS

Numerical simulations are conducted with the Pressure Acoustics module of COMSOL Multiphysics. The single-layer numerical model for impedance metasurfaces[47] is adopted for the numerical simulations shown in Fig. 3. The impedance matrix is defined by Eqs. (14)–(17). The sidewalls of the two waveguides are set with hard acoustic boundary conditions. Their length is set to $3\lambda_0$, with upper and lower boundaries set with plane wave radiation boundary conditions. The mesh has a maximum element size of $\lambda_0/10$ and a minimum element size of $\lambda_0/15$ for convergence, and the discretization uses quadratic Lagrange elements. All numerical simulations are performed with a background pressure field for excitation, with the pressure distribution defined by Eqs. (12) and (13). It should be mentioned that phase differences are set arbitrarily as $\varphi_{l_1,m}=0$, $\varphi_{l_2,m}=\pi/3$, and $\varphi_{l_3,m}=\pi/4$ to avoid singularities.

The numerical simulation in Fig. 4(b) uses the same configuration, but replaces the single-layer numerical model with the practical structure, and the waveguide radius at the input side is set to 7.5 cm. All other settings, including mesh, discretization, and quantitative evaluation, are the same as in Fig. 3.

APPENDIX C: QUANTITATIVE EVALUATION

The Galerkin method is adopted for both the simulation and experimental results to retrieve the amplitude of each CBM without integration. Any acoustic field inside a waveguide can be expressed in series form as

$$\begin{aligned} p(\rho,\theta,z)&=\sum_l\sum_m p_{l,m}(\rho,\theta,z)\\ &=\sum_l\sum_m D_{l,m}J_m(\beta_{l,m}\rho)\mathrm{e}^{-\imath\alpha_{l,m}z-\imath m\theta-\imath\varphi_{l,m}}\\ &=\sum_{s=1}^{(2|m|+1)l}p_s\mathrm{e}^{-\imath\varphi_s}f_s(\rho,\theta,z). \end{aligned} \tag{C1}$$

The sampled data $\tilde{p}(\rho_\xi,\theta_\xi,z_\xi)$ at the ξth sampling point located at $(\rho_\xi,\theta_\xi,z_\xi)$ obey

$$\tilde{p}(x_\xi,y_\xi)=\sum_{s=1}^{(2|m|+1)l}p_s\mathrm{e}^{-\imath\varphi_s}f_s(\rho_\xi,\theta_\xi,z_\xi). \tag{C2}$$

By repeating the sampling t times, the following system of equations can be established:

$$\begin{bmatrix} f_1(x_1,y_1) & \cdots & f_{(2|m|+1)l}(x_1,y_1)\\ \vdots & \vdots & \vdots\\ f_1(x_\xi,y_\xi) & \cdots & f_{(2|m|+1)l}(x_\xi,y_\xi)\\ \vdots & \vdots & \vdots\\ f_1(x_t,y_t) & \cdots & f_{(2|m|+1)l}(x_t,y_t)\end{bmatrix}\begin{bmatrix} p_1\mathrm{e}^{-\imath\varphi_1}\\ \vdots\\ p_{(2|m|+1)l}\mathrm{e}^{-\imath\varphi_{(2|m|+1)l}}\end{bmatrix}=\begin{bmatrix}\tilde{p}(x_1,y_1)\\ \vdots\\ \tilde{p}(x_\xi,y_\xi)\\ \vdots\\ \tilde{p}(x_t,y_t)\end{bmatrix}' \tag{C3}$$

which can be abbreviated as

$$\mathbf{Ax}=\mathbf{b}. \tag{C4}$$

When $t\geq(2|m|+1)l$, Eq. (C3) has a least squares solution

$$\mathbf{x}=\mathbf{A}^+\mathbf{b}. \tag{C5}$$

The complex amplitude of each CBM can then be retrieved. All sampling points are used for the Galerkin method in the experiment. For the field on each side of the metasurface in the simulation, the sampling region consists of two parallel planes located at distances of $1.5\lambda_0$ and $1.6\lambda_0$ from the metasurface. On each plane, 20 sampling points are uniformly distributed along the radial direction

24 October 2026 16:30:23

© Author(s) 2026

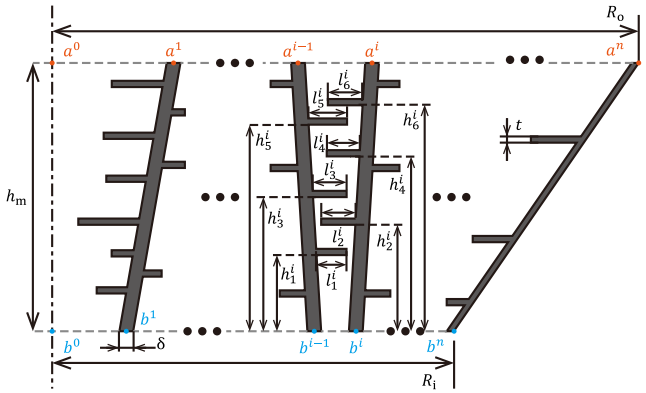


FIG. 5. Schematic of designed generalized acoustic impedance metasurface.

and 30 points along the azimuthal direction, forming a polar grid. This yields a total of 20 × 30 × 2 sampling points, which are used to extract the complex amplitudes of each CBM.

The performances of all metasurface can then be evaluated by power flux conversion. The wave field p_1 is divided into two parts, incidence p_{in} and reflection p_{re}, as follows:

$$p_1 = p_{in} + p_{re}. \tag{C6}$$

The normal incident power flux can then be calculated as

$$I_{in,z} = -\mathbf{n}_1 \cdot \frac{1}{2}\mathrm{Re}\,[p_{in}\mathbf{v}_{in}^*]. \tag{C7}$$

It should be noted that p_{in} is not a simple plane wave for the incident field excited by the nonplanar excitation in the experiment. The normal power flux allocated to mode $\{l, m\}$ is given by

$$I_{l,m,z} = \mathbf{n}_2 \cdot \frac{1}{2}\mathrm{Re}\,[p_{l,m}\mathbf{v}_{l,m}^*]. \tag{C8}$$

Consequently, the conversion rate is given by

$$\eta_{l,m} = \frac{I_{l,m,z}}{I_{in,z}}. \tag{C9}$$

This equation is applicable for both simulation and experiment.

APPENDIX D: OPTIMIZATION AND PARAMETERS OF DESIGNED GENERALIZED ACOUSTIC IMPEDANCE METASURFACES

A schematic of the designed generalized acoustic impedance metasurface is shown in Fig. 5. The thick black dashed line represents the central axis of the rotating body. The gray solid part is the rotating section. The light gray dashed line is the port where each unit connects the incident and reflected fields. The radii of the upper and lower surfaces are R_o = 15 cm and R_i = 7.5 cm, respectively. The thickness of the metasurface is h_m = 8 cm. The division of the units is carried out along the radial direction from the origin point. The upper surface is first divided into patches at intervals of 0.5 cm. Taking the total normal power flow on each patch as a reference, the lower surface is then divided in sequence while ensuring conservation between each pair of patches on both surfaces. For the purpose of fabrication with 3D printing, adjacent patches are allow to be combined according to the following rules. First, the width of the lower surface patch should be greater than 0.3 cm. Second, the maximum width of the unit should not exceed 3 cm (i.e., the deeply sub-wavelength) condition, so that its impedance matrix is uniquely determined. Third, the area ratio of the patches at both surfaces is equal to the ratio of off-diagonal components of the target impedance matrix defined by the midpoints:

$$\begin{bmatrix} p_1|_{(b^i-b^{i-1})/2} \\ p_2|_{(a^i-a^{i-1})/2} \end{bmatrix} = \begin{bmatrix} \imath X_{11}^i & \imath X_{12}^i \\ \imath X_{21}^i & \imath X_{22}^i \end{bmatrix} \begin{bmatrix} (-\mathbf{n}_1 \cdot \mathbf{v}_1)|_{(b^i-b^{i-1})/2} \\ (-\mathbf{n}_2 \cdot \mathbf{v}_1)|_{(a^i-a^{i-1})/2} \end{bmatrix}. \tag{D1}$$

It should be noted that the impedance of the first unit is defined by the origin point. The division of units is recorded in columns 2 and 3 of Tables II and III. It should also be noted that a^7 in Table II corresponds to two different values. This is because the widths of the seventh and eighth units have already reached 3 cm, and the normal power flow on the patch between these two units is quite low. This patch cannot either be merged into adjacent units or become an independent one, to avoid violating the rules mentioned above. It is therefore skipped.

Structural design of the impedance unit is implemented through parameter optimization based on a genetic algorithm. There is a $\delta/2$ = 0.1 cm gap at each side of the unit for the purpose of isolation. Six plates each of thickness t = 0.2 cm are added to each unit

TABLE II. Parameter configuration of the metasurface for case 1 (cm).

i	a^i	b^i	h_1^i	h_2^i	h_3^i	h_4^i	h_5^i	h_6^i	l_1^i	l_2^i	l_3^i	l_4^i	l_5^i	l_6^i
0	0.00	0.00	⋯	⋯	⋯	⋯	⋯	⋯	⋯	⋯	⋯	⋯	⋯	⋯
1	1.00	1.24	1.49	2.82	3.28	3.58	3.88	4.93	0.56	0.71	0.40	0.45	0.47	0.52
2	2.00	2.41	1.06	2.17	3.75	4.05	5.34	6.30	0.12	0.67	0.73	0.30	0.70	0.45
3	3.00	3.47	1.62	2.74	3.81	4.25	5.49	6.69	0.41	0.68	0.51	0.67	0.66	0.37
4	4.00	4.37	0.28	1.66	1.98	3.69	4.45	6.25	0.15	0.31	0.57	0.59	0.43	0.62
5	5.00	5.08	1.46	2.93	3.28	4.10	4.53	5.55	0.42	0.46	0.48	0.50	0.53	0.56
6	6.00	5.59	1.15	2.74	4.76	5.06	5.97	6.27	0.23	0.33	0.45	0.48	0.52	0.55
7	9.00(−) 10.00(+)	6.07	2.27	2.71	3.69	4.15	4.99	5.29	0.84	0.55	1.29	0.20	0.51	0.59
8	13.00	6.60	2.13	3.33	4.89	5.19	5.49	6.08	0.83	1.26	1.68	1.21	1.87	0.92
9	15.00	7.50	0.92	1.45	2.92	4.24	4.61	5.50	0.67	0.77	0.95	0.72	1.18	1.33

24 October 2026 16:30:23

© Author(s) 2026

TABLE III. Parameter configuration of the metasurface for case 2 (cm).

i	a^i	b^i	h_1^i	h_2^i	h_3^i	h_4^i	h_5^i	h_6^i	l_1^i	l_2^i	l_3^i	l_4^i	l_5^i	l_6^i
0	0.00	0.00	...	...	...	...	...	...	...	...	...	...	...	...
1	1.66	1.00	0.18	2.01	2.41	3.61	5.88	6.30	0.59	0.81	0.82	0.74	0.19	0.22
2	3.03	2.00	2.51	3.61	4.31	4.69	5.21	6.06	0.65	0.74	0.72	0.72	0.70	0.69
3	3.97	3.00	2.94	4.63	5.47	5.79	6.39	6.69	0.40	0.67	0.66	0.66	0.17	0.65
4	4.49	5.00	1.00	1.90	2.80	3.26	4.29	5.63	0.37	0.53	0.71	0.78	0.98	0.56
5	5.06	7.50	1.34	2.59	2.89	3.58	4.21	5.01	0.59	0.94	0.96	1.18	1.28	1.52
6	6.30	9.50	1.03	2.27	3.14	3.55	4.31	5.79	1.03	1.17	1.23	0.78	1.34	1.33
7	6.70	12.00	0.92	2.16	4.62	5.65	6.65	7.48	0.34	0.71	1.31	1.63	1.84	1.51
8	7.03	14.00	1.55	2.27	2.67	3.25	4.50	5.13	0.35	0.15	0.58	0.36	0.74	0.54
9	7.50	15.00	2.37	2.77	3.17	4.24	5.43	5.83	0.32	0.23	0.12	0.39	0.44	0.37

as shown in Fig. 5. The six plates in the first unit are attached to the outer wall, while those in other units are arranged in sequence with three on each side. The height and the length of the jth plate from the lower boundary in the ith unit are h_j^i and l_j^i, respectively. These 12 parameters are selected as the optimization variables to approach the target impedance matrix. The detailed optimization results for the two cases are recorded in columns 4–15 of Tables II and III, respectively.

APPENDIX E: INFLUENCE OF DISCRETIZATION OF UNITS ON EFFICIENCY

To discuss the influence of unit discretization on efficiency, a numerical model for generalized impedance metasurfaces is established as shown in Fig. 6(a). The pseudo-real expression of the impedance matrix[49] combined with the three-layer numerical model[46] is used to describe metasurfaces. The metasurface is divided

24 October 2026 16:30:23

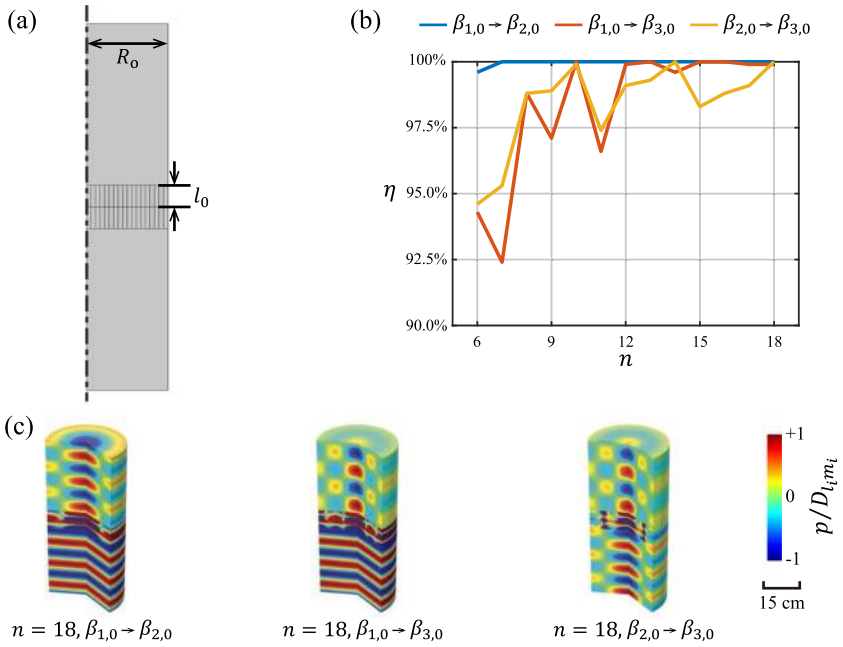


FIG. 6. Simulation results for the influence of different unit discretizations on metasurface efficiency. (a) Three-layer numerical model for simulation. (b) Influence of different numbers of discrete units on the efficiency of metasurfaces for $\beta_{1,0} \to \beta_{2,0}$ (blue line), $\beta_{1,0} \to \beta_{3,0}$ (orange line), and $\beta_{2,0} \to \beta_{3,0}$ (yellow line). (c) Simulation results for metasurfaces with $n = 18$.

© Author(s) 2026

equally into n three-layer units whose impedance components are determined by

$$\left[\begin{matrix} p_1 \\ p_2 \end{matrix}\right]\Big|_{y=0} = \left[\begin{matrix} R_{11}+X_{11} & X_{12} \\ X_{12} & X_{22} \end{matrix}\right]\left[\begin{matrix} (-\mathbf{n}_1\cdot\mathbf{v}_1) \\ (-\mathbf{n}_2\cdot\mathbf{v}_2) \end{matrix}\right]\Big|_{y=0}. \tag{E1}$$

Each unit is composed of two waveguides with a length of $l_0 = h_m/2$ and three interior impedance boundaries determined by

$$Z_1 = R_{11} + \imath X_{11} + \imath X_{12} + \imath Z_0 \cot(k_0 l_0), \tag{E2}$$

$$Z_2 = 2\imath Z_0 \cot(k_0 l_0) - \frac{Z_0^2}{\imath X_{12}} \sin^{-2}(k_0 l_0), \tag{E3}$$

$$Z_3 = \imath X_{22} + \imath X_{12} + \imath Z_0 \cot(k_0 l_0). \tag{E4}$$

An interior acoustic hard boundary is set between adjacent units for isolation. Other settings, including background media, operating frequency, plane wave radiation boundary, and mesh, are consistent with the previous discussion.

Numbers of discrete units ranging from 6 to 18 are considered, and the operating efficiency of the metasurface is shown in Fig. 6(b). It can be seen that when the number of units exceeds 9, the efficiency is always greater than 95%. The efficiency of the metasurfaces for $\beta_{1,0} \to \beta_{2,0}$ is always close to 100%. However, for $\beta_{1,0} \to \beta_{3,0}$, more discretization is needed to provide better results. It should be noted that owing to the presence of zero-points in the CBM amplitude, some impedance matrices may become singular. Therefore, there may still be an abnormal decrease in efficiency, although the number of discrete units is increased. This is even more pronounced in the metasurfaces for $\beta_{2,0} \to \beta_{3,0}$. Therefore, the selection of unit positions should also be taken into account in metasurface design. In any case, the generalized impedance metasurfaces are always capable of performing CBM modulation when sufficient discretization is ensured, as shown in Fig. 6(c). All normalized transmission fields are consistent with the ideal results in Fig. 3.

APPENDIX F: EXPERIMENTAL SETUP

The entire experimental setup is placed in a fully anechoic chamber, as shown in Fig. 7. Signals generated and collected in the experiment are controlled by a B&K 3160-A-042 control module connected to a computer. Metasurfaces are fabricated from a photosensitive resin, and waveguides on both side are composed of polylactic acid (PLA), which can be regarded as rigid in air. The exit of the output waveguide is covered by a sound-absorbing foam to avoid reflection. Two intersecting square areas with a side length of 29 cm, placed 5 cm away from the metasurface, are selected as the measuring areas for sampling of the output signal. There are 29×29 evenly distributed points, with a sampling spacing of 1 cm. Two intersecting rectangular areas with a length of 29 cm and a width of 14 cm, placed 5 cm away from the speaker, are selected as the measuring areas for sampling of the input signal, and 29×14 evenly distributed points with a spacing of 1 cm are adopted.

APPENDIX G: OPERATING FREQUENCIES

The frequency-domain responses of metasurfaces for $\beta_{1,0} \to \beta_{2,0}$ and $\beta_{1,0} \to \beta_{3,0}$ are shown in Figs. 8(a) and 8(b), respectively.

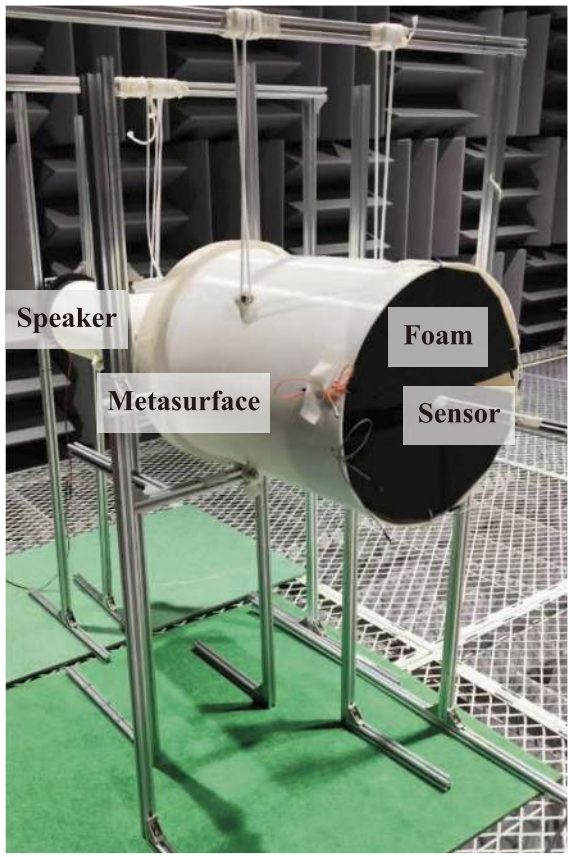


FIG. 7. Experimental setup for generation with a single speaker.

The model used for simulation is consistent with the previous discussion, but the air domain in the metasurface is governed by the thermoviscous acoustic equation. It should be noted that owing to the introduction of viscosity, the peak points of operating efficiency are shifted toward lower frequencies. However, an efficiency over 60% can be guaranteed within the 500 Hz range near the operating frequency. In addition, although the power allocated to the target CBM is relatively low, the transmitted field is pure. It can be observed that the efficiency of total transmission and the efficiency allocated to the target CBM are always close. The generalized impedance metasurface shows an obvious function as a filter, which promises great potential for its application in acoustic communication.

APPENDIX H: INFLUENCE OF NONPLANAR EXCITATION

The influences of nonplanar excitation for both metasurfaces are now discussed. The Dirichlet condition at the entrance of the waveguide with $p = 1$ is set as the excitation, instead of the background pressure field. This implies that the superposition of incident and reflected waves at the entrance is equal to 1. Therefore, this model can be used to estimate the impact of reflection on the surface of the speaker. The air domain in the metasurface is governed

24 October 2026 16:30:23

© Author(s) 2026

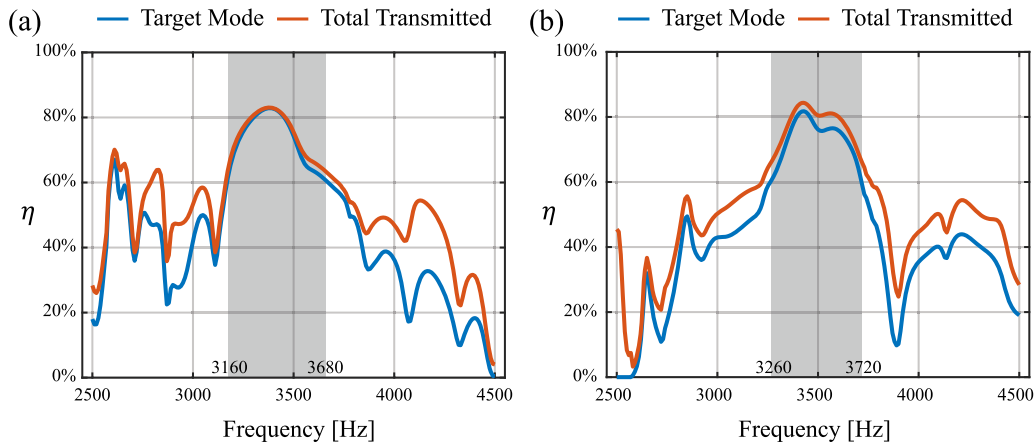


FIG. 8. Frequency-domain response of metasurfaces for (a) $\beta_{1,0} \rightarrow \beta_{2,0}$ and (b) $\beta_{1,0} \rightarrow \beta_{3,0}$.

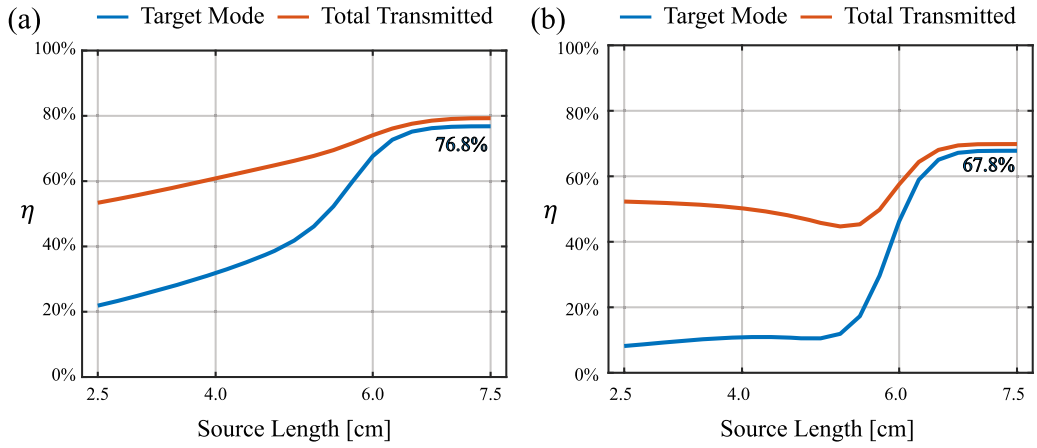


FIG. 9. Simulation results for the influence of different lengths of sound source on the efficiency of metasurfaces for (a) $\beta_{1,0} \rightarrow \beta_{2,0}$ and (b) $\beta_{1,0} \rightarrow \beta_{3,0}$.

by the thermoviscous acoustic equation. Other settings of the simulation model are consistent with those in Fig. 4(b). The length of the sound source is set to vary from 2.5 to 7.5 cm. The simulation results for metasurfaces with $\beta_{1,0} \rightarrow \beta_{2,0}$ and $\beta_{1,0} \rightarrow \beta_{3,0}$ are shown in Figs. 9(a) and 9(b), respectively.

It can be seen that owing to the nonplanarity of the excitation, the operating efficiencies of both metasurfaces are significantly reduced. Even if the source completely covers the waveguide entrance with a length of 7.5 cm, the excitation efficiency of the target CBM still decreases to 76.8% and 67.8% for the cases with $\beta_{1,0} \rightarrow \beta_{2,0}$ and $\beta_{1,0} \rightarrow \beta_{3,0}$, respectively. This phenomenon is basically consistent with the experimental results. However, only a small portion of power leaks out of the target CBM mode, when the length of the sound source is greater than 6 cm. The purity of the transmitted field can be guaranteed because of the filtering of generalized impedance metasurfaces.

REFERENCES

[1] I. F. Akyildiz, C. Han, Z. Hu, S. Nie, and J. M. Jornet, "Terahertz band communication: An old problem revisited and research directions for the next decade," IEEE Trans. Commun. **70**, 4250 (2022).
[2] H. Luo, J. Wang, F. Bu, R. Ruby, K. Wu, and Z. Guo, "Recent progress of air/water cross-boundary communications for underwater sensor networks: A review," IEEE Sens. J. **22**, 8360 (2022).
[3] J. Durnin, "Exact solutions for nondiffracting beams. I. The scalar theory," J. Opt. Soc. Am. A **4**(4), 651–654 (1987).
[4] J. Durnin, J. J. Miceli, Jr, and J. H. Eberly, "Diffraction-free beams," Phys. Rev. Lett. **58**(15), 1499 (1987).
[5] A. B. Valyaev and S. G. Krivoshlykov, "Mode properties of Bessel beams," Sov. J. Quantum Electron. **19**(5), 679–680 (1989).
[6] G. Guo, X. Li, Q. Wang, Y. Li, H. Chu, Q. Ma, J. Tu, and D. Zhang, "Spectrum decomposition-based orbital angular momentum communication of acoustic vortex beams using single-ring transceiver arrays," IEEE Trans. Ultrason. Ferroelectr. Freq. Control. **68**(4), 1399–1407 (2021).

24 October 2026 16:30:23

© Author(s) 2026

[7]X. Li, Y. Li, Q. Ma, G. Guo, J. Tu, and D. Zhang, "Principle and performance of orbital angular momentum communication of acoustic vortex beams based on single-ring transceiver arrays," J. Appl. Phys. **127**(12), 124902 (2020).
[8]S. Gao, Y. Li, C. Ma, Y. Cheng, and X. Liu, "Emitting long-distance spiral airborne sound using low-profile planar acoustic antenna," Nat. Commun. **12**(1), 2006 (2021).
[9]H.-T. Zhou, S.-C. Zhang, T. Zhu, Y.-Z. Tian, Y.-F. Wang, and Y.-S. Wang, "Hybrid metasurfaces for perfect transmission and customized manipulation of sound across water–air interface," Adv. Sci. **10**(19), 2207181 (2023).
[10]X.-D. Fan, Z. Zou, and L. Zhang, "Acoustic vortices in inhomogeneous media," Phys. Rev. Res. **1**(3), 032014 (2019).
[11]R. D. Muelas-Hurtado, J. L. Ealo, and K. Volke-Sepúlveda, "Active-spiral Fresnel zone plate with tunable focal length for airborne generation of focused acoustic vortices," Appl. Phys. Lett. **116**(11), 114101 (2020).
[12]Y. Wang, J. Qian, J.-P. Xia, Y. Ge, S.-Q. Yuan, H.-X. Sun, and X.-J. Liu, "Acoustic Bessel vortex beam by quasi-three-dimensional reflected metasurfaces," Micromachines **12**(11), 1388 (2021).
[13]J. Zhang, Z. Lin, J. Liu, J. Liu, Z. Lin, S. Mo, S. Lin, L. Shen, L. Zhang, Y. Chen *et al.*, "SDM transmission of orbital angular momentum mode channels over a multi-ring-core fibre," Nanophotonics **11**(4), 873–884 (2022).
[14]Y. Lian, Y. Yu, S. Han, N. Luan, Y. Wang, and Z. Lu, "OAM beams generation technology in optical fiber: A review," IEEE Sens. J. **22**(5), 3828–3843 (2022).
[15]L. Tong, Z. Xiong, Y.-X. Shen, Y.-G. Peng, X.-Y. Huang, L. Ye, M. Tang, F.-Y. Cai, H.-R. Zheng, J.-B. Xu *et al.*, "An acoustic meta-skin insulator," Adv. Mater. **32**(37), 2002251 (2020).
[16]Y. Fu, C. Shen, X. Zhu, J. Li, Y. Liu, S. A. Cummer, and Y. Xu, "Sound vortex diffraction via topological charge in phase gradient metagratings," Sci. Adv. **6**(40), eaba9876 (2020).
[17]X. Jiang, Y. Li, B. Liang, J.-C. Cheng, and L. Zhang, "Convert acoustic resonances to orbital angular momentum," Phys. Rev. Lett. **117**(3), 034301 (2016).
[18]C. Liu, Y. Ye, and J. H. Wu, "An asymmetric generator of acoustic vortex with high-purity," Int. J. Mech. Sci. **261**, 108695 (2024).
[19]J. F. Pazos-Ospina, J. L. Ealo, and E. E. Franco, "Characterization of phased array-steered acoustic vortex beams," J. Acoust. Soc. Am. **142**(1), 61–71 (2017).
[20]A. Marzo, M. Caleap, and B. W. Drinkwater, "Acoustic virtual vortices with tunable orbital angular momentum for trapping of Mie particles," Phys. Rev. Lett. **120**(4), 044301 (2018).
[21]Z. Li, Q. Zhang, F. Qu, Y. Wei, X. Tu, J. Xu, W. Xu, and L. Yang, "High-speed underwater acoustic orbital angular momentum communications," IEEE J. Oceanic Eng. **49**, 1588 (2024).
[22]C. Shi, M. Dubois, Y. Wang, and X. Zhang, "High-speed acoustic communication by multiplexing orbital angular momentum," Proc. Natl. Acad. Sci. **114**(28), 7250–7253 (2017).
[23]W. Lu, H. Sun, Y. Lan, and R. Guo, "Generation of topologically diverse acoustic vortex beams with same divergence angle using discrete active helical arrays," J. Appl. Phys. **130**(6), 064501 (2021).
[24]F. Ju, Y. Cheng, and X. Liu, "Acoustic spin Hall-like effect in hyperbolic metamaterials controlled by the helical wave," Sci. Rep. **8**(1), 11113 (2018).
[25]C. Shi, R. Zhao, Y. Long, S. Yang, Y. Wang, H. Chen, J. Ren, and X. Zhang, "Observation of acoustic spin," Natl. Sci. Rev. **6**(4), 707–712 (2019).
[26]Y. Long, H. Ge, D. Zhang, X. Xu, J. Ren, M.-H. Lu, M. Bao, H. Chen, and Y.-F. Chen, "Symmetry selective directionality in near-field acoustics," Natl. Sci. Rev. **7**(6), 1024–1035 (2020).
[27]S. Li and J. Wang, "Multi-orbital-angular-momentum multi-ring fiber for high-density space-division multiplexing," IEEE Photonics J. **5**(5), 7101007 (2013).
[28]Y.-Z. Tian, X.-L. Tang, Y.-F. Wang, V. Laude, and Y.-S. Wang, "Annular acoustic impedance metasurfaces for encrypted information storage," Phys. Rev. Appl. **20**(4), 044053 (2023).
[29]B. Assouar, B. Liang, Y. Wu, Y. Li, J.-C. Cheng, and Y. Jing, "Acoustic metasurfaces," Nat. Rev. Mater. **3**(12), 460–472 (2018).
[30]A.-L. Chen, Y.-S. Wang, Y.-F. Wang, H.-T. Zhou, and S.-M. Yuan, "Design of acoustic/elastic phase gradient metasurfaces: Principles, functional elements, tunability, and coding," Appl. Mech. Rev. **74**(2), 020801 (2022).
[31]Y.-F. Wang, Y.-Z. Wang, B. Wu, W. Chen, and Y.-S. Wang, "Tunable and active phononic crystals and metamaterials," Appl. Mech. Rev. **72**(4), 040801 (2020).
[32]L. Meng, F. Cai, F. Li, W. Zhou, L. Niu, and H. Zheng, "Acoustic tweezers," J. Phys. Appl. Phys. **52**(27), 273001 (2019).
[33]N. Yu, P. Genevet, M. A. Kats, F. Aieta, J.-P. Tetienne, F. Capasso, and Z. Gaburro, "Light propagation with phase discontinuities: Generalized laws of reflection and refraction," science **334**(6054), 333–337 (2011).
[34]Y. Li, B. Liang, Z.-M. Gu, X.-Y. Zou, and J.-C. Cheng, "Reflected wavefront manipulation based on ultrathin planar acoustic metasurfaces," Sci. Rep. **3**(1), 2546 (2013).
[35]Y. Xie, W. Wang, H. Chen, A. Konneker, B.-I. Popa, and S. A. Cummer, "Wavefront modulation and subwavelength diffractive acoustics with an acoustic metasurface," Nat. Commun. **5**(1), 5553 (2014).
[36]X. Jiang, B. Liang, J.-C. Cheng, and C.-W. Qiu, "Twisted acoustics: Metasurface-enabled multiplexing and demultiplexing," Adv. Mater. **30**(18), 1800257 (2018).
[37]Y. Ra'di, D. L. Sounas, and A. Alù, "Metagratings: Beyond the limits of graded metasurfaces for wave front control," Phys. Rev. Lett. **119**(6), 067404 (2017).
[38]D. Torrent, "Acoustic anomalous reflectors based on diffraction grating engineering," Phys. Rev. B **98**(6), 060101 (2018).
[39]X. Jiang, J. Zhao, S.-L. Liu, B. Liang, X.-Y. Zou, J. Yang, C.-W. Qiu, and J.-C. Cheng, "Broadband and stable acoustic vortex emitter with multi-arm coiling slits," Appl. Phys. Lett. **108**(20), 203501 (2016).
[40]Z. Hou, H. Ding, N. Wang, X. Fang, and Y. Li, "Acoustic vortices via nonlocal metagratings," Phys. Rev. Appl. **16**(1), 014002 (2021).
[41]X.-R. Li, Y.-R. Jia, Y.-C. Luo, J. Yao, and D.-J. Wu, "Mixed focused-acoustic-vortices generated by an artificial structure plate engraved with discrete rectangular holes," Appl. Phys. Lett. **118**(4), 043503 (2021).
[42]Z.-K. Cheng, M.-C. Luo, X.-Y. Sun, M. Chen, Y. Zhang, S.-Q. Li, and X.-C. Zhu, "Observation of the rotational doppler shift of a spinning object based on an acoustic vortex with a Fresnel-spiral zone plate," J. Appl. Phys. **133**(11), 114502 (2023).
[43]K. Wu, J.-J. Liu, Y.-J. Ding, W. Wang, B. Liang, and J.-C. Cheng, "Metamaterial-based real-time communication with high information density by multipath twisting of acoustic wave," Nat. Commun. **13**(1), 5171 (2022).
[44]Y. Fu, Y. Tian, X. Li, S. Yang, Y. Liu, Y. Xu, and M. Lu, "Asymmetric generation of acoustic vortex using dual-layer metasurfaces," Phys. Rev. Lett. **128**(10), 104501 (2022).
[45]M. Farhat, P.-Y. Chen, and Y. Wu, "Sound waveguiding by spinning: An avenue toward unidirectional acoustic spinning fibers," Phys. Rev. Appl. **19**(4), L041002 (2023).
[46]A. Díaz-Rubio and S. A. Tretyakov, "Acoustic metasurfaces for scattering-free anomalous reflection and refraction," Phys. Rev. B **96**(12), 125409 (2017).
[47]M. Jiang, Y.-F. Wang, B. Assouar, and Y.-S. Wang, "Scattering-free modulation of elastic shear-horizontal waves based on interface-impedance theory," Phys. Rev. Appl. **20**(5), 054020 (2023).
[48]Y.-Z. Tian, Z.-R. Wei, Y.-F. Wang, V. Laude, and Y.-S. Wang, "Adjustable phase-amplitude-phase acoustic metasurface for the implementation of arbitrary impedance matrices," Research **7**, 0502 (2024).
[49]Y.-Z. Tian, Y.-F. Wang, V. Laude, and Y.-S. Wang, "Generalized acoustic impedance metasurface," Commun. Phys. **7**(1), 34 (2024).

24 October 2026 16:30:23

© Author(s) 2026